metals

MDPI

Article

On the $M_{23}C_6$-Carbide in 2205 Duplex Stainless Steel: An Unexpected ($M_{23}C_6$/Austenite)—Eutectoid in the δ-Ferritic Matrix

Abdelkrim Redjaïmia [1,2,*] and Antonio Manuel Mateo Garcia [3]

[1] Institut Jean Lamour UMR CNRS 7198, Université de Lorraine, F-54011 Nancy, France
[2] Laboratory of Excellence "Design of Alloy Metals for Low-Mass Structures" (DAMAS), Université de Lorraine, F-57070 Metz, France
[3] Department of Materials Science and Metallurgical Engineering, Campus Diagonal Besòs-EEBE, Universitat Politecnica de Catalunya, 08019 Barcelona, Spain; antonio.manuel.mateo@upc.edu
* Correspondence: Abdelkrim.redjaimia@univ-lorraine.fr; Tel.: +33-03-7274-2722

Abstract: This study is focused on isothermal and anisothermal precipitation of $M_{23}C_6$ carbides from the fully ferritic structure of the (γ + δ) austenitic-ferritic duplex stainless steel X2CrNiMo2253, (2205). During isothermal heat treatments, small particles of K-$M_{23}C_6$ carbide precipitates at the δ/δ grain-boundaries. Their formation precedes γ and σ-phases, by acting as highly potential nucleation sites, confirming the undertaken TEM investigations. Furthermore, anisothermal heat treatment leads to the formation of very fine islands dispersed throughout the fully δ-ferritic matrix. TEM characterization of these islands reveals a particular eutectoid, reminiscent of the well-known (γ-σ)—eutectoid, usually encountered in this kind of steel. TEM and electron microdiffraction techniques were used to determine the crystal structure of the eutectoid constituents: γ-Austenite and K-$M_{23}C_6$ carbides. Based on this characterization, orientation relationships between the two latter phases and the ferritic matrix were derived: cube-on-cube, on one hand, between K-$M_{23}C_6$ and γ-Austenite and Kurdjumov-Sachs, on the other hand, between γ-Austenite and the δ-ferritic matrix. Based on these rational orientation relationships and using group theory (symmetry analysis), the morphology and the only one variant number of K-$M_{23}C_6$ in γ-Austenite have been elucidated and explained. Thermodynamic calculations, based on the commercial software ThermoCalq® (Thermo-Calc Software, Stockholm, Sweden), were carried out to explain the K-$M_{23}C_6$ precipitation and its effect on the other decomposition products of the ferritic matrix, namely γ-Austenite and σ-Sigma phase. For this purpose, the mole fraction evolution of K-$M_{23}C_6$ and σ-phase and the mass percent of all components entering in their composition, have been drawn. A geometrical model, based on the corrugated compact layers instead of lattice planes with the conservation of the site density at the interface plane, has been proposed to explain the transition δ-ferrite ⇒ {γ-Austenite ⇔ K-$M_{23}C_6$}.

Keywords: duplex stainless steels; $M_{23}C_6$ carbide; crystal structure; ($M_{23}C_6$/γ)-eutectoid; morphology; geometrical model; mechanism; thermodynamic calculations

Citation: Redjaïmia, A.; Mateo Garcia, A.M. On the $M_{23}C_6$-Carbide in 2205 Duplex Stainless Steel: An Unexpected ($M_{23}C_6$/Austenite)—Eutectoid in the δ-Ferritic Matrix. *Metals* **2021**, *11*, 1340. https://doi.org/10.3390/met11091340

Academic Editor: Francesca Borgioli

Received: 13 July 2021
Accepted: 19 August 2021
Published: 25 August 2021

1. Introduction

Duplex stainless steels (DSS) are increasingly used from the eighties of the past century as structural material in oil, chemical and power industries [1–4]. This is related to the fact that their duplex microstructure (γ + δ) allows a beneficial mixture of γ-austenitic and δ-ferritic properties, leading to, on the one hand, high strength with a desirable toughness [5,6] and, on the other hand, good corrosion resistance, especially to chloride-induced stress corrosion cracking [7–9]. The X2CrNiMo2253 DSS, with nominal composition (wt.%) Fe-22Cr-5Ni-3Mo-0.03C, is a member of this family. This grade is largely used as a standard material in offshore conditions [10], and it is usually designed as 2205 in reference to its chromium (22 wt.%) and nickel (5 wt.%) contents. The heat treatment of this DSS leads to a

series of metallurgical transformations, which take place in ferrite or at its grain boundaries, apart from the martensite, which forms in the austenite grains [11–18]. In a detailed study [19,20], efforts were made to characterize the different products of the δ-ferritic matrix decomposition in the temperature range 400–1050 °C. The characterization of the phase precipitation was best undertaken by an isothermal heat treatment from the fully δ-ferritic microstructure retained by water-quenching to ambient temperature, from the solutionising single domain. This isothermal heat treatment induces the decomposition of the supersaturated δ-ferrite. The various identified phases include the M_7C_3 and $M_{23}C_6$ carbides [11–20], the γ-Austenite with its different morphologies [19–21], the α′-ferrite [11,22] being responsible for the well-known embrittlement at 475 °C in Fe-Cr system [23–25], the intermetallic G-phase [26,27], the τ-phase [28–30] and also undesirable secondary precipitates. The latter are the intermetallic phases: σ-sigma [31–35], χ-chi [36–39] and *R* phase [40–43], the well-known Frank-Kasper phases [44].

Practical crystallographic data of the most commonly encountered phases, in the 2205-DSS, are gathered in Table 1. It can be noticed that:

- the lattice parameter of K-$M_{23}C_6$ is three times that of γ-austenite,
- the capital letter *M* usually stands for Cr and Fe but it can also include other substitution elements such as Mo and/or W, elements promoting the carbide formation,
- for typographic simplifications, the $M_{23}C_6$ carbide, will be labelled, in this study, K-carbide or K-$M_{23}C_6$, as needed. The austenite and the ferrite will be labelled γ-austenite and δ-ferrite (δ-matrix), respectively.

Through this study, crystallographic, microstructural and thermodynamic aspects will be addressed to support the formation of this unexpected ($M_{23}C_6$/austenite)-eutectoid.

Table 1. Crystallographic characteristics of the phases encountered in the 2205-DSS by the decomposition of the fully ferritic matrix, during isothermal heat treatment.

Phase	Lattice Type	Space Group	Lattice Paremeters (nm)	Atom Number (cell)	References (*), (***)
δ, α′	BCC	$Im\bar{3}m$	a = 0.2867	2	–
γ, γ_P	FCC	$Fm\bar{3}m$	a = 0.3539	4	–
$M_{23}C_6$	FCC	$Fm\bar{3}m$	a = 1.0645	116 { M = 92; C = 24 }	[11–13] This study
σ	Tetragonal	$P4_2/mnm$	{ a = 0.8800; c = 0.4583 }	30	[31,33–35]
χ	BCC	$I\bar{4}3m$	a = 0.8920	58	[36–38]
G	FCC	$Fm\bar{3}m$	a = 1.1484	116	[26,27]
R	Trigonal	$R\bar{3}$	{ { a = 0.8959; α = 74°30′ } { a = 1.0903; c = 1.9342 } }	53 (Rhombohedral) 3 × 53 = 159 (Hexagonal)	[40–43]
τ	Orthorhombic	Fmmm	a = 0.4055 b = 0.4667 c = 0.2867	4	[28,29]

(*) First identified by and (***) characterised by X-ray, neutron and/or electron diffraction techniques.

2. Materials and Methods

The chemical composition of 2205-DSS used for this investigation is given in Table 2. The as-received (γ + δ) state had a balanced microstructure with 50% γ and 50% δ (Figure 1a). It was solution treated at 1375 °C for 20 min to achieve homogeneity and subsequently water-quenched (WQ) to retain a supersaturated and fully δ-ferritic microstructure (Figure 1b). After this fully ferritisation, isothermal and anisothermal heat treatments were conducted on parallelepipedal strips with dimensions of 30 mm × 20 mm × 2 mm. For

the former, specimens were heat treated in the temperature range 500–1150 °C for various times up to 336 h (2 weeks), followed by water-cooling; while for the latter, they were subjected to a continuous cooling from the single δ-ferritic domain (Figure 1b), directly to the room temperature with a powerful air-jet. It can be underlined here that the cooling rate was, unfortunately, not quantified, but easily reproducible. In this case, the cooling rate is slower than that used for water-quenching but much faster than that used for air cooling. All the heat treatments were carried out in electric muffle furnaces under vacuum to minimize, as much as possible, the oxidation process.

Table 2. Chemical composition of the as-received material and of the fully ferritic state.

Elements (wt. %)	Fe	Cr	Ni	Mo	Mn	Si	C	N
As-received	balance	22.5	5.1	2.5	1.6	0.5	0.03	0.08
$\delta-$ferrite (1375 °C, WQ)	balance	22.74	5.01	2.55	1.63	0.46	-	-

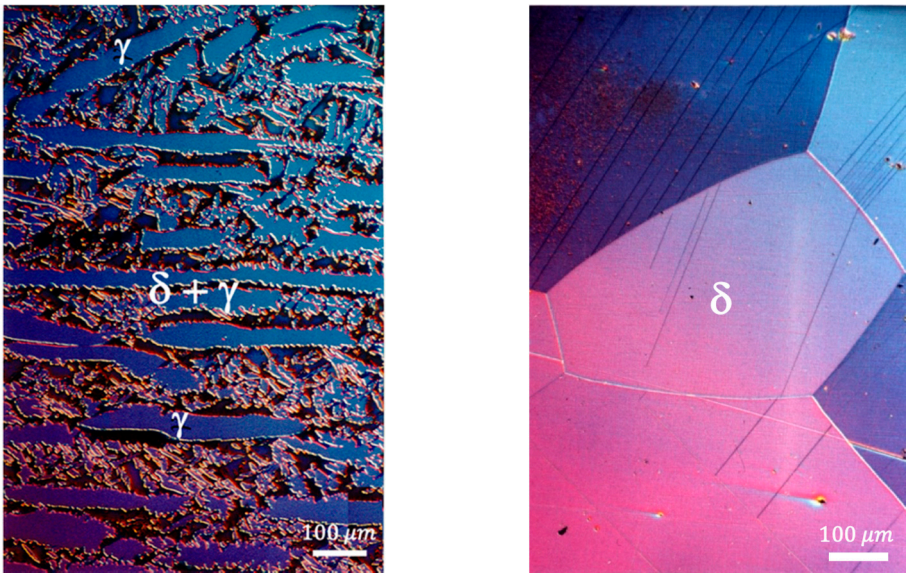

(**a**) (**b**)

Figure 1. Light microscopy images of the 2205-DSS: (**a**) as-received material with a duplex (δ-ferrite + γ-austenite) microstructure (50%/50%), (**b**) supersaturated fully δ-ferritic microstructure obtained by ferritisation at 1375 °C during 20 min, subsequently followed by water quenching (WQ). The presence of black parallel streaks can be noticed in δ-ferritic grains (**b**). These streaks are mechanical twins, called Neumann bands.

Metallographic preparation of the specimens, for the different characterizations, was performed; that involved standardized metallographic mounting and polishing techniques, while etching after polishing on diamond pads was performed with electrolytic etching at 4 V NaOH in 100 mL distilled water. The mole fractions versus temperature/time of the decomposition products of the ferritic matrix are given in details elsewhere [19,20].

Thin foils for transmission electron microscopy (TEM) were prepared following conventional TEM specimen preparation methods. The specimens were mechanically ground down to the lowest possible thickness (20–10 μm) and then electro-polished at 40 V in a solution of 5% perchloric acid in 95% II-butoxy-ethanol, employing a Struers Tenupol twin-jet unit.

Specimen examination was performed on a Philips CM12 Microscope with an acceleration voltage of 120 kV. Diffraction patterns were obtained in the selected area electron diffraction (SAED) mode with a parallel incident beam and especially in the microdiffraction mode, using convergent beam electron diffraction (CBED) with a nearly parallel electron beam focused on a very small area of the thin analysed foils (10 nm).

An X-ray diffractometer, with Co-Kα radiation, was used to determine with accuracy the lattice parameter of the body-centered cubic (bcc) ferritic matrix. This lattice parameter was used as a calibration to index the recorded electron diffraction patterns and to deduce the lattice parameters of the decomposition products of the ferritic matrix, notably carbides.

3. Results

3.1. Isothermal Intergranular Precipitation of K-$M_{23}C_6$

In the early stage of the δ-ferrite decomposition, $M_{23}C_6$ particles appear at the δ/δ grain boundaries. Figure 2a shows a bright field TEM image with a chaplet of these carbide particles growing on one side of the δ/δ grain boundaries. This intergranular precipitation prior to the decomposition of the other intermetallic products is attributed to the great mobility of the carbon atoms towards the high energy δ/δ grain boundaries enriched in carbides forming elements, essentially chromium and molybdenum.

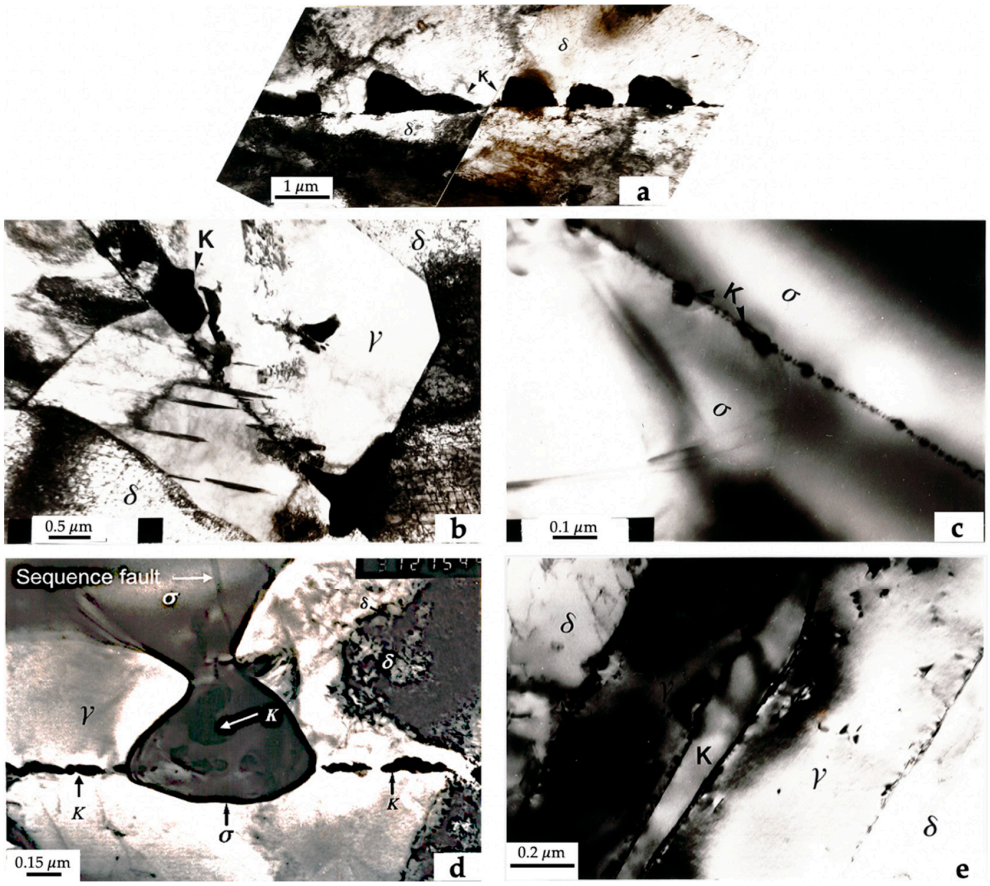

Figure 2. Bright field TEM images of the 2205-DSS of the intergranular precipitation of K-$M_{23}C_6$: (**a**) as a particles chaplet on the δ/δ grain boundary, (**b**) δ/δ intergranular chaplet embedded in γ-phase, (**c**) δ/δ intergranular chaplet embedded in σ-phase, (**d**) δ/δ intergranular particles chaplet serving as nucleation sites for both γ and σ phases, and (**e**) platelet of K-$M_{23}C_6$ taking place inside the γ-phase. The black streaks in (**b**) are twins in the austenite crossing of the δ/δ grain boundary. High dislocation density around the austenite island (**b**) is also noteworthy, as the sequence faults inside the σ-phase (**b**,**c**).

TEM investigations show that the intergranular K-$M_{23}C_6$ particles are, most of the time, embedded in σ-phase (Figure 2c,d) and remain insoluble over a long period, up to 336 h. This confirms the fact that carbon is insoluble in σ-phase and the in-situ transformation is highly unlikely, contrary to what is claimed in the literature [39].

The bright field TEM images (Figure 2b,d) show intergranular $M_{23}C_6$ particles inserted in austenite islands. The precipitation of $M_{23}C_6$ particles leads to the impoverishment

in chromium and enrichment in nickel around the δ/δ grain boundaries, promoting the austenite island formation. The K-$M_{23}C_6$ carbides may also precipitate as platelets in the austenite, as shown in Figure 2e.

The precipitation of those carbides, and the corresponding in chromium depletion around the δ/δ grain boundaries, locally reduce the resistance of the δ-ferrite matrix to oxidation, inducing the embrittlement of the steel.

Owing to the fact that the $M_{23}C_6$ particles act as nucleation sites for σ-sigma and γ-austenite, it was potentially expected that rational orientation relationships would develop. Unfortunately, it was very difficult to record any orientation relationships between the very small δ/δ-grain boundaries, the $M_{23}C_6$ particles and the σ-sigma or the γ-phase, where they were embedded.

3.2. Anisothermal Intragranular Precipitation of K-$M_{23}C_6$

In addition to the inter and intra-granular austenite formation in ferrite, an aggregate type, whose microstructure is not well resolved by light microscopy, takes place at the δ/δ and δ/γ interfaces and within the δ-ferritic grains (Figure 3b–d). This aggregate, with different dimensions, up to 15 µm, dispersed inside the ferritic grains and displaying a like-eutectoid morphology evokes the well-known (σ-γ)-eutectoid morphology mentioned in the same DSS [19,20].

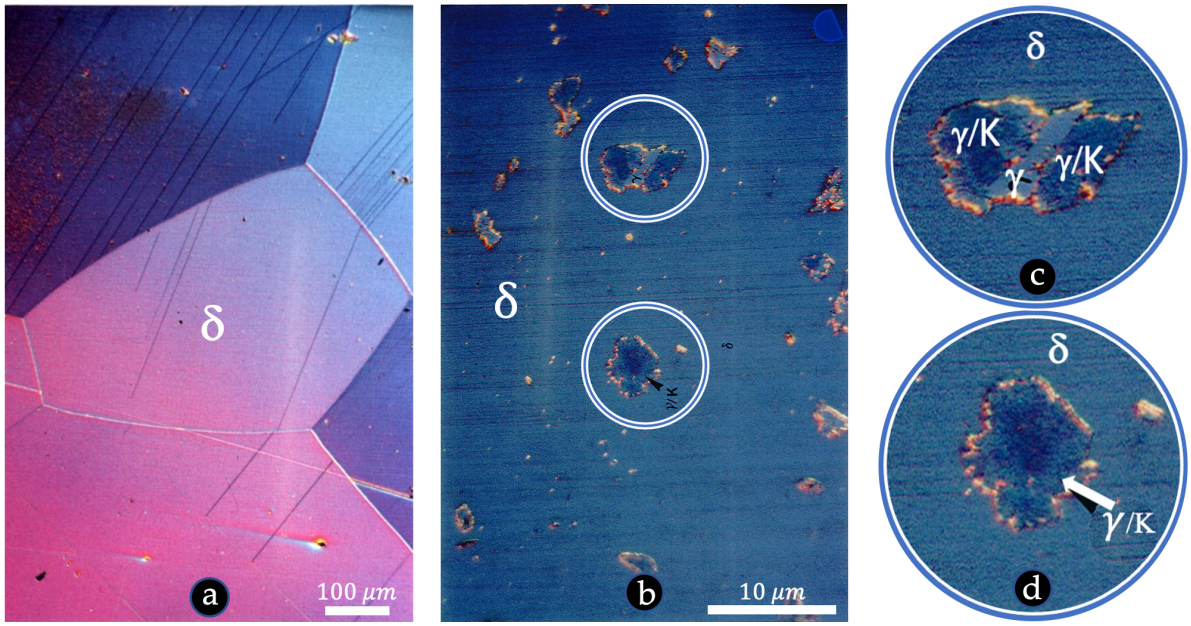

Figure 3. Light microscopy images of the 2205-DSS: (**a**) supersaturated fully δ-ferritic structure obtained by ferritisation at 1375 °C during 20 min, subsequently followed by water quenching. One can notice the presence of black parallel streaks in the fully δ-ferritic grains. These streaks are twins, also called Neumann bands, (**b**) a like-eutectoid morphology (K-$M_{23}C_6$, γ-austenite) embedded in the δ-ferritic matrix. Microstructure obtained after a continuous cooling from the fully ferritic state. Light microscopy images of the nodule with a like-eutectoid morphology. One can notice that some austenite-nodules are noticeably free of carbide, (**c**,**d**) enlarged parts of image (**b**): (**c**) (K-γ)-eutectoid nodules in a twinned γ-austenite, and (**d**) one variant of K/γ.

Through a detailed study in TEM (Figure 4), it turns out that, in this eutectoid, the alternated lamellae are different from those found in the (σ-γ)-eutectoid, as mentioned previously [19,20]. In addition, bright and dark field TEM images reveal that these aggregates consist, in fact, on alternating lamellae of carbide and austenite. The carbide-lamellae of an aggregate are all connected together, forming a continuous network (Figure 4b,c), a unique variant in the γ-austenitic nodule. This particular behaviour will be explained in detail in the next section. Another important point is concerned with the volume fraction of the aggregates which stays limited during the anisothermal heat treatment.

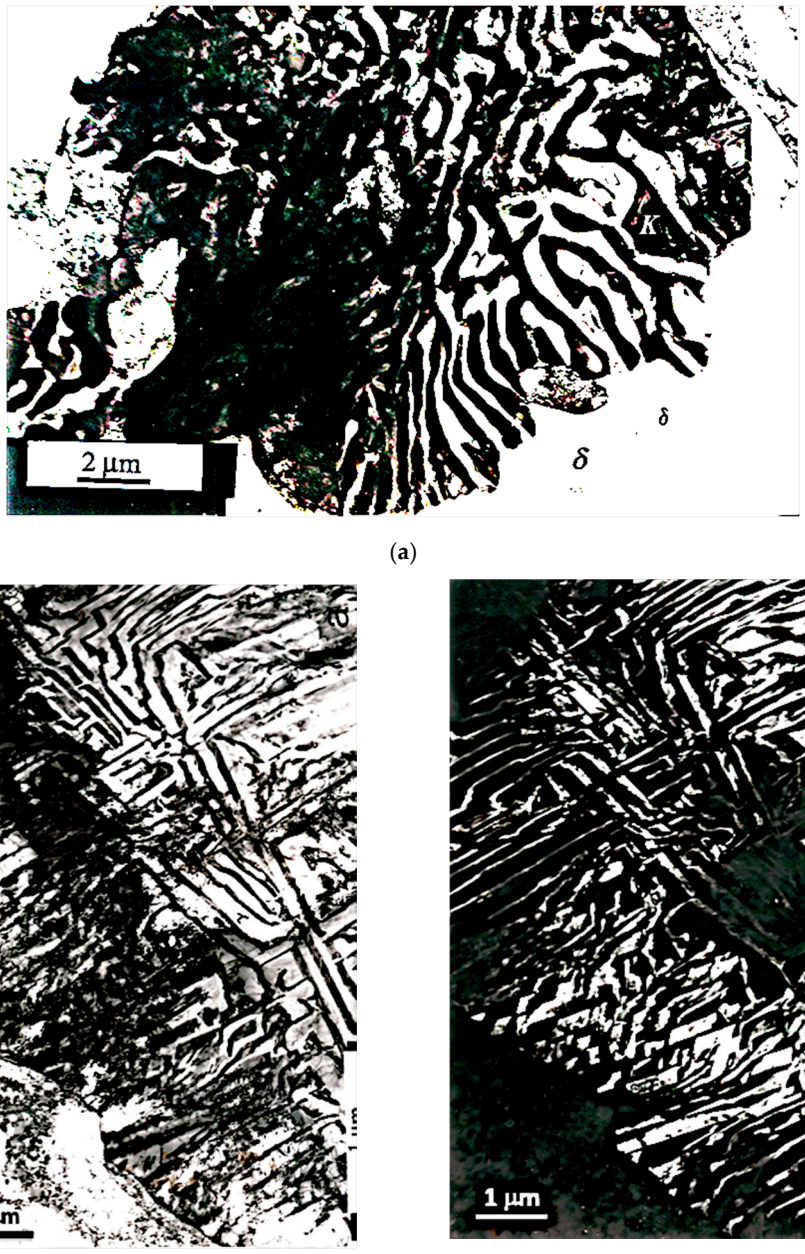

(**a**)

(**b**) (**c**)

Figure 4. (**a**) Bright field TEM image of the nodule with a like-eutectoid morphology, embedded in the δ-ferritic matrix, (**b**) bright and (**c**) dark field TEM images of K-$M_{23}C_6$ network in the γ-austenitic nodule embedded in the δ-ferritic matrix. The K-$M_{23}C_6$ is a unique variant in the γ-austenitic nodule.

As far as we are aware, it is the first time such an aggregate has been identified in DSS during an anisothermal heat treatment. The crystal structure (space group and lattice parameters) of this constituent will be identified in the following section, using the electron diffraction technique.

3.3. Identification of the Crystal Structure of the Constituent of the Eutectoid, the K-Carbide

To confirm the nature of the found aggregate, and to decide in favour of one or the other of the two eutectoids (σ-γ) or (K-γ), a detailed characterization study was conducted by electron diffraction, leading to resolve the crystallographic structure. In doing so, electron microdiffraction was used to identify the crystal structure of the K-carbide lamellae, the orientation relationship between austenite and the K-carbide and also to know about its link with the ferritic matrix.

Due the size of the carbide particles precipitating in the ferritic matrix, the X-ray diffraction is not relevant. However, Transmission Electron Microscopy (TEM image, Selected Area Electron Diffraction (SAED) and Microdiffraction modes) is therefore qualified and used to identify the crystal structure and to explain the morphology developed by the carbides during the isothermal and anisothermal heat treatments, from the fully ferritic matrix.

A microdiffraction pattern corresponds to the intersection of the Ewald sphere with the zeroth and first reciprocal lattice layers recorded along ⟨uvw⟩, a zone axis of the phase to identify. To these zeroth and first layers correspond the Zero (ZOLZ) and the First (FOLZ) Order Laue Zones, respectively (Figure 5).

Microdiffraction analysis is based on the net and ideal symmetries of the ZOLZ and of the Whole Pattern, WP = (ZOLZ + FOLZ) [45–52]. The net symmetry is concerned with the position of reflections while the ideal symmetry is linked to both the position and the intensity of these reflections. These symmetries, observed along specific zone axes, are connected to the crystal systems and to the symmetry point groups. The shift between the ZOLZ and FOLZ reflection nets is related to the Bravais lattice [45–52] (Figure 5), while the periodicity difference between the ZOLZ and FOLZ reflection nets is in connection with the presence of glide planes [45–52]. Taking into account both the shift and the difference periodicity between the ZOLZ and the FOLZ coupled to the Bravais lattice (crystal system) and to the symmetry point group leads to the individual extinction symbol [53,54]. Addition of the individual extinction symbols obtained along at least three zone axes gives the partial extinction symbol [50,55]. To the latter belong one or a few space groups [49–52].

The procedure using the electron microdiffraction technique is summarised jointly in Figure 5 and Table 3.

Table 3. Derivation of space group in relation with the symmetry of diffraction patterns.

Ideal Symmetry of WP (ZOLZ+FOLZ)	Possible Point Groups	Possible Crystal Systems ZAP	Possible Individual Extinction Symbols	Possible Space Group
{(4mm), 4mm}	$\frac{4}{m}\frac{2}{m}\frac{2}{m}$	Tetragonal [001]	I − ...	$I\frac{4}{m}\frac{2}{m}\frac{2}{m}$, $I\frac{4}{m}\frac{2}{c}\frac{2}{m}$
	4mm			I4mm, I4am $I4_1md$, $I4_1cd$
	$\frac{4}{m}\bar{3}\frac{2}{m}$	Cubic ⟨001⟩	I − ...	$I\frac{4}{m}\bar{3}\frac{2}{m}$
			F − ...	$F\frac{4}{m}\bar{3}\frac{2}{m}$, $F\frac{4}{m}\bar{3}\frac{2}{c}$

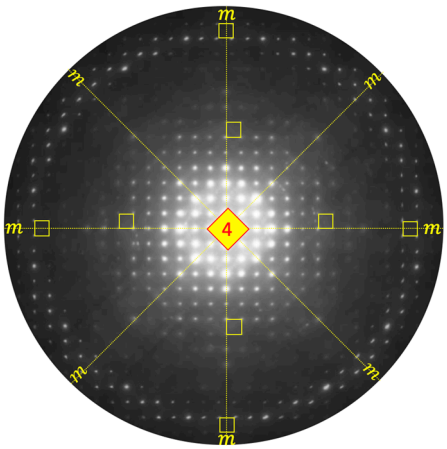

Figure 5. Electron microdiffraction pattern exhibiting {(4mm); 4mm} ideal symmetry leading in (Table 3) to three possible point groups and 9 possible space groups grouped in two possible crystal systems, cubic (3 space groups) or tetragonal (6 space groups).

Based on the microdiffraction technique, we now proceed to the crystal identification of the K-carbide. Indeed, Figure 6a–c exhibits microdiffraction patterns recorded along three different zones axes (ZAPs). Taking into account both the position and the intensity of the reflections of these ZAPs, it is clear that the highest ideal symmetries (The notation for the "net" and "ideal" symmetries of the ZOLZ and of the Whole Pattern (WP) and for the partial extinction symbols are given in accordance with those used in reference [49].), for this phase, are {(4mm); 4mm}, {(2mm); 2mm} and {(6mm); 3m}, respectively. Considering these symmetries, it can be inferred that the K-phase crystallizes in the cubic system and belongs to the holohedric $m\bar{3}m$ point group, the highest symmetry point group [53,54] and the three diffraction patterns are recorded along ⟨001⟩, ⟨111⟩ and ⟨110⟩ ZAPs types, respectively [49–51].

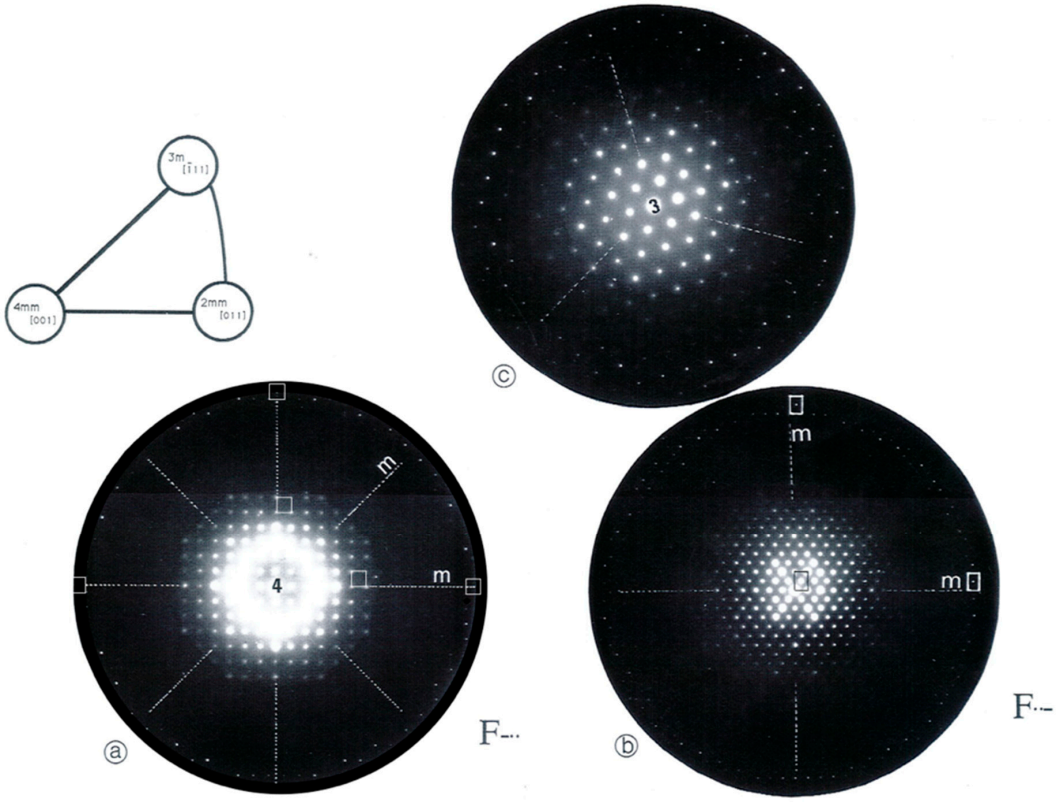

Figure 6. Electron microdiffraction patterns of K-carbide showing: (**a**) {(4mm); 4mm}, (**b**) {(2mm); 2mm} and (**c**) {(6mm); 3m} ideal symmetries recorded along [001], [011] and [$\bar{1}$11] zone axes, respectively.

The absence of (ZOLZ)/(FOLZ) a periodicity difference along both [001] and [011] axes (Figure 6a,b) indicates that there is no glide plane perpendicular to these two directions and the partial extinction symbol is F− − − [53,54]. Based on the derived m$\bar{3}$m point group and F− − − extinction symbol, it can be concluded, without any ambiguity, that the K-phase crystallizes in the cubic system with the face centred Bravais lattice (fcc) and belongs to the space group Fm$\bar{3}$m (No. 225) or F$\frac{4}{m}\bar{3}\frac{2}{m}$, in its full notation [53,54].

The ferritic matrix parameter, $a_\alpha = 0.2867$ nm, characterised by X-ray diffraction, is used to calibrate the electron diffraction patterns and to deduce the lattice parameters of the cubic K-phase, namely, $a_K = 1.0645$ nm.

From the F$\frac{4}{m}\bar{3}\frac{2}{m}$ space group and the lattice parameter $a_K = 1.0645$ nm, determined from electron diffraction patterns recorded along different zone axes, it is confirmed that the K-phase, together with the γ-austenite, is effectively one of the two constituents of the lamellar eutectoid. The latter is composed with alternated γ-austenite and carbide lamellae.

3.4. Orientation Relationship (OR) between the K-$M_{23}C_6$ and the γ-Austenite in the Eutectoid Nodule

Based on the diffraction patterns recorded along (a) $[001]_K//[001]_\gamma$, (b) $[112]_K//[112]_\gamma$ and (c) $[011]_K//[011]_\gamma$ zones axes (Figure 7), it is experimentally obvious that K-$M_{23}C_6$ have a definite orientation relationship with respect to the γ-austenite and consequently with the δ-ferritic matrix in which the (K-γ)-eutectoid nodules take place. The triperiodically overlapping of spots arising from the K-$M_{23}C_6$ and γ-austenite indicates that many lattice planes from the two phases are parallel and have identical three time interplanar spacing. It can be concluded without ambiguity that the K-$M_{23}C_6$ is a supercell of the γ-austenite; the unit cell of the $M_{23}C_6$ carbide is described here as a triperiodic stacking of $(3 \times 3 \times 3) = 27$ unit cells of austenite. This would favor an easy epitaxial nucleation and growth of the K-$M_{23}C_6$ from the γ-austenite.

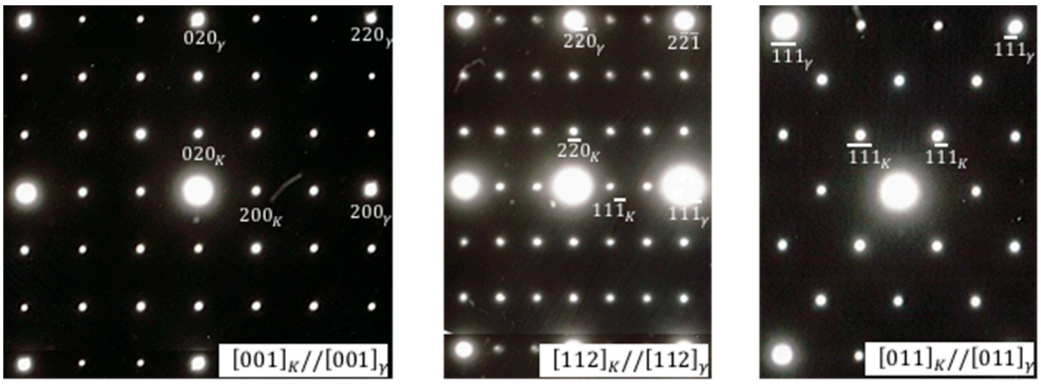

(**a**) (**b**) (**c**)

Figure 7. Series of selected Area Electron Diffraction patterns (SAED) recorded along: (**a**) $[001]_K//[001]_\gamma$, (**b**) $[112]_K//[112]_\gamma$ and (**c**) $[011]_K//[011]_\gamma$, leading to a cube-on-cube orientation relationship between K-$M_{23}C_6$ and γ-austenite.

The derived orientation relationship expressed by exact parallelism between the corresponding planes and exact parallelism between directions lying in these planes is labelled a cube-on-cube orientation relationship. Due to the fact that the γ-austenite develops a Kurdjumov-Sachs orientation relationship [56] with the δ-ferritic matrix, it can be established that a triangular orientation relationship (TOR) is developed and can be quoted and gathered in the following Table 4.

Table 4. Triangular orientation relationship (TOR) between: K-$M_{23}C_6$, γ-austenite and the δ-ferritic matrix.

Phases	**K−$M_{23}C_6$**	**γ−Austenite**	**δ−ferrite**
Space groups	$Fm\bar{3}m\left(F\frac{4}{m}\bar{3}\frac{2}{m}\right)$	$Fm\bar{3}m\left(F\frac{4}{m}\bar{3}\frac{2}{m}\right)$	$Im\bar{3}m\left(I\frac{4}{m}\bar{3}\frac{2}{m}\right)$
Lattice parameters	$a_K = 1.062$ nm	$a_\gamma = 0.354$ nm	$a_\delta = 0.287$ nm
Orientation relationships	Cube − on − cube	Kurdjumov − Sachs	Kurdjumov − Sachs
	$(001)_K//(001)_\gamma$ $(110)_K//(110)_\gamma$ $(111)_K//(111)_\gamma$	$(110)_\delta//(111)_\gamma$ $[1\bar{1}1]_\delta//[\bar{1}10]_\gamma$ $[\bar{1}12]_\delta//[11\bar{2}]_\gamma$	$(110)_\delta//(111)_K$ $[1\bar{1}1]_\delta//[\bar{1}10]_K$ $[\bar{1}12]_\delta//[11\bar{2}]_K$
Triangular Orientation Relationship (TOR)		$(111)_K//(111)_\gamma//(110)_\delta$ $[\bar{1}10]_K//[\bar{1}10]_\gamma//[1\bar{1}1]_\delta$ $[11\bar{2}]_K//[11\bar{2}]_\gamma//[\bar{1}12]_\delta$	

The identification of this rational orientation relationships between the matrix and its decomposition products is an important step in the morphological characterization which will be displayed in the next paragraph.

3.5. Symmetry Analysis and Morphology, the Equilibrium Shape

It is well established, through group theory, that the morphology of phases, taking place in any medium (solid, liquid or gas) is of great importance in materials science.

Both the morphology and the variant number of the precipitate, which adopts orientation relationships with the matrix, can be understood in terms of group theory [57,58]. This symmetry concept has been successfully applied to determine the number of variants and to characterize the morphology of precipitates in different alloy systems, and is widely investigated [59–66]. This approach, based on the shared symmetry elements of the two point groups can be applied to explain the habitus and especially the variant number developed by the K-$M_{23}C_6$ in the eutectoid nodule. It is well known that the shape of a crystallographic precipitate developing in a solid matrix is dictated by the point group, labelled H_h, whose elements are common to the precipitate and to the matrix point groups [57,58]. The H_h point group is one of the *32* crystallographic point groups and *h* is its group order [57,58].

Based on the electron diffraction patterns (Figure 7a–c) and the derived cube-on-cube orientation relationship, the 4, 3 and 2-fold rotation axes and the inversion centres, common to the K-$M_{23}C_6$ phase and to the γ-austenite, survive to the intersection point group (Table 5a). It is therefore clear that the shared symmetry elements lead to the intersection point group H_h:

$$H_h = G_{48}^{K} \cap G_{48}^{\gamma} = \frac{4}{m}\bar{3}\frac{2}{m} \cap \frac{4}{m}\bar{3}\frac{2}{m} = \frac{4}{m}\bar{3}\frac{2}{m}$$

The resulting point group $H_{48} = \frac{4}{m}\bar{3}\frac{2}{m}$ is the cubic point group, whose order is 48 [53,54]. It dictates the shape of K-$M_{23}C_6$ carbide. For this point group, the general forms developed are (hkl)-hexoctahedra and the special ones are (100)-cubic, (110)-rhombic dodecahedron, (hk0)-tetrahexahedra, (111)-octahedra, (hll)-icositetrahedra, and (hhl)-trisoctahedra [53,54]. All these shapes correspond to an absolute extremum [57].

Whatever the shape developed by the K-$M_{23}C_6$ phase, it corresponds to an absolute extremum [57]. The equilibrium shape, which is consistent with the one experimentally, observed, elongated along $[1\bar{1}0]_{K,\,\gamma} \parallel [1\bar{1}1]_{\delta}$ direction (Figure 8) is energetically favourable, i.e., it is a stable carbide.

Table 5. Derivation of the intersection point group H, whose symmetry elements are common to: (**a**)The γ-austenite and the K-carbide related by a cube-on-cube orientation relationship. The K-carbide developed 1 variant in the γ-austenite. (**b**) The γ-austenite and the δ-ferrite related by a Kurdjumov-Sachs orientation relationship. The γ-austenite developed 24 variants in the δ-ferritic matrix.

	Point Groups ⇓	**Orientation Relationships**	**Superimposition of Symmetry Elements**	**Shared Symmetry Elements**	**Variant Numbers n = m/h**
a	$G_{48}^{K} = \frac{4}{m}\bar{3}\frac{2}{m}$ $G_{48}^{\gamma} = \frac{4}{m}\bar{3}\frac{2}{m}$	Cube − on − cube		$H_h^{K/\gamma} = \left(G_{48}^{K} \cap G_{48}^{\gamma}\right)$ $H = \frac{4}{m}\bar{3}\frac{2}{m}$ $h = 48$	$n = \frac{48}{48}$ $n = 1$
		$(001)_K // (001)_\gamma$	$\frac{4}{m} // \frac{4}{m} = \frac{4}{m}$		
		$(111)_K // (111)_\gamma$	$\bar{3} // \bar{3} = \bar{3}$		
		$(110)_K // (110)_\gamma$	$\frac{2}{m} // \frac{2}{m} = \frac{2}{m}$		
b	$G_{48}^{\gamma} = \frac{4}{m}\bar{3}\frac{2}{m}$ $G_{48}^{\delta} = \frac{4}{m}\bar{3}\frac{2}{m}$	Kurdjumov − Sachs		$H_h^{\gamma/\delta} = \left(G_{48}^{\gamma} \cap G_{48}^{\delta}\right)$ $H = \bar{1}$ $h = 2$	$n = \frac{48}{2}$ $n = 24$
		$(110)_\delta // (111)_\gamma$	$\frac{2}{m} // \bar{3} = \bar{1}$		
		$(1\bar{1}1)_\delta // (\bar{1}10)_\gamma$	$\bar{3} // \frac{2}{m} = \bar{1}$		
		$(\bar{1}12)_\delta // (11\bar{2})_\gamma$	$1 // 1 = 1$		

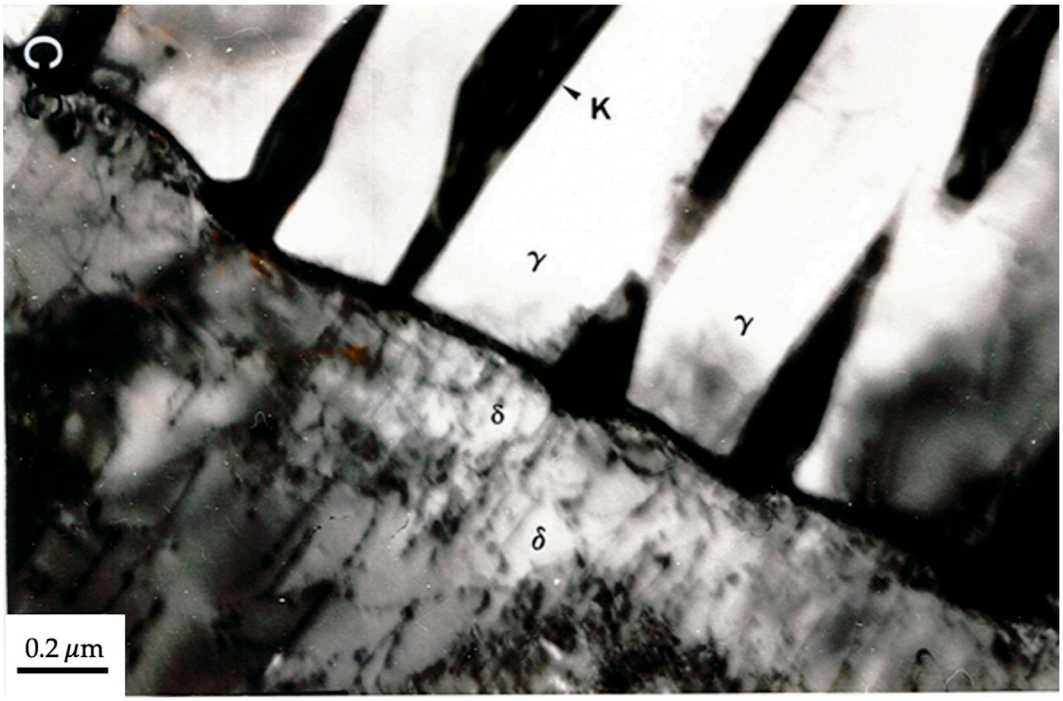

Figure 8. Bright field TEM image, recorded along $[111]_{K,\gamma} \parallel [110]_{\delta}$, displaying the development of (K-$M_{23}C_6$/γ-austenite)-eutectoid in the δ-ferritic matrix. The K-$M_{23}C_6$ takes place at the interface δ/γ and grows inside the γ-austenite nodule along the $[1\bar{1}0]_{K,\gamma} \parallel [1\bar{1}1]_{\delta}$ directions.

Defined as the index of H_{48} in G^{γ}_{48}, the number of variants n is the ratio of the order of G^{γ}_{48} to that of H_{48}, i.e., n = 48/48 = 1 [57,58]. This means that for the K-$M_{23}C_6$, there is only 1 variant that could take place in every grain of austenite. The derivation procedure of the point group H_h, sharing the symmetry elements between both K-$M_{23}C_6$/γ-austenite and γ-austenite/δ-ferrite, is summarised in Table 5a.

Based on the triangular orientation relationship (TOR) between the three phases, symmetry analysis asserts that, in every ferritic grain, 24 austenite variants (nodule) are developed and in each one, one K-$M_{23}C_6$ variant takes place in the γ-austenite (Table 5b).

This result is the answer to the raised question in Section 3.2 about the origin of the carbide lamellae connected together, forming a continuous network (Figure 4b,c) in the ($M_{23}C_6$/γ-austenite)-eutectoid.

3.6. Passage: δ-Ferrite ⇒ γ-Austenite ⇒ K-$M_{23}C_6$: Geometrical Model

The $M_{23}C_6$, as the γ-austenite, crystallises in the fcc structure and belongs to the space group $Fm\bar{3}m$, with a lattice parameter $a_k = 1.062$ nm ($a_k = 3a_\gamma = 3 \times 0.354$ nm).

The $M_{23}C_6$ carbide (M = atomic metals, Cr, Fe, etc.) is described by a conventional unit cell with four inequivalent metal sites, namely, the 4a, 8c, 32f, and 48h sites, according to Wyckoff notation [55]. The carbon atoms (C) are located at the 24e sites [55] (Table 6).

Table 6. Position of atoms in the unit cell of the $M_{23}C_6$ carbide.

Atom Number (Site) (Wyckoff Notation)	Local Site Symmetry	Atom Nature	Fractional Atom Coordinates		
			x	y	z
4(a)	$m\bar{3}m$	Cr	0.00000	0.00000	0.00000
8(c)	$\bar{4}3m$	Cr	0.25000	0.25000	0.25000
32(f)	.3m	Cr	0.38500	0.38500	0.38500
48(h)	m.m2	Cr	0.00000	0.16500	0.16500
24(e)	4m.m	C	0.00000	0.00000	0.25600

The $M_{23}C_6$ carbide structure can also be described as a packing of polyhedra: cubo-octahedral and cubic groups [67–71]. These atomic groups, labelled P and Q (Polyhedral and Stick Modes, CrystalMaker®) (CrystalMaker Software Ltd., Oxford, UK) constitute the motif of the fcc structure and are located at {0, 0, 0} and {1/2, 0, 0} site types of the unit cell [67–71], respectively. The cuboctahedron is a polyhedron with 8 triangular faces and 6 square faces parallel to {111} and {001} planes of the unit cell, respectively. Each square face shares its sides with 4 triangular faces. The sites are parallel to <110> unit cell directions. The faces of the cubic groups are orthogonal to the <001> directions of the carbide unit cell (Figure 9).

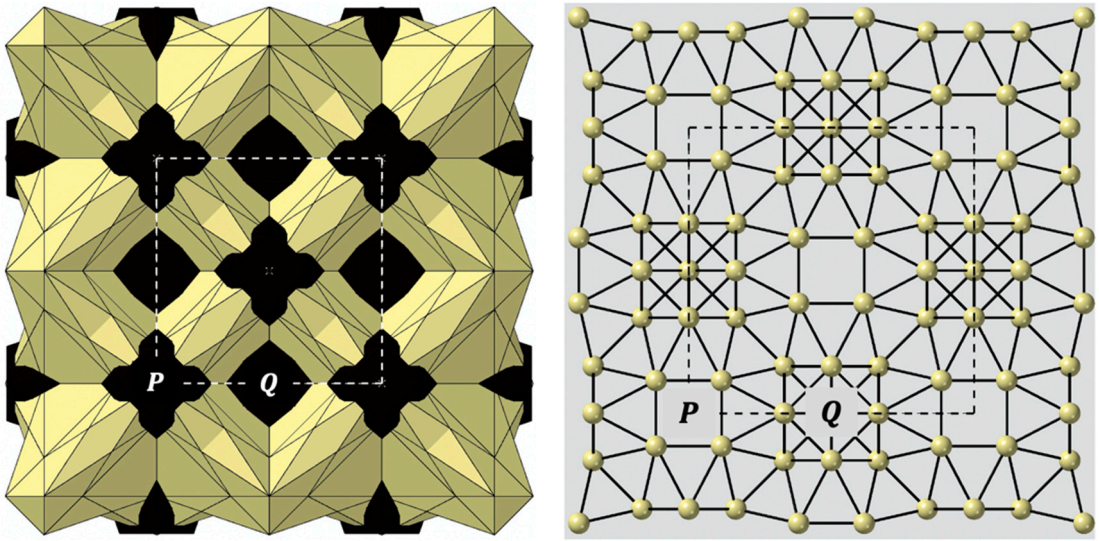

(**a**) Polyhedral mode (CrystalMaker®) (**b**) Stick mode (CrystalMaker®)

Figure 9. Crystal structure of the fcc $M_{23}C_6$ carbide observed along [001] showing packing of atoms organised in polyhedra: cubo-octahedra and cubes, located at (0, 0, 0) and (1/2, 0, 0) sites, labelled P and Q, respectively (CrystalMaker®, (**a**) polyhedral and (**b**) stick modes).

In the case of carbides with simple structures, such as the fcc-VC or hcp-Mo_2C (hexagonal close packed), the atomistic mechanism underlying the ORs with the austenite is easily explained by their lattice correspondence relationship [68]. These are discussed in with respect of matching of individual atoms on the interface between the engaged two phases, the carbide and the austenite. However, in the case of the $M_{23}C_6$ and M_6C complex carbides, matching between individual metal atoms on the interface is not so obvious and must be examined in detail, in order to obtain a plausible explanation of the respective OR.

In the present study, the possible pairing of metal atoms through the interface developed by the K-$M_{23}C_6$ with both the austenite and the ferrite, will be tackled by setting up a geometric model.

Based on the triangular orientation relationship and the trace analysis, let us draw crystallographic planes of the three phases namely, $(111)_K//(111)_\gamma//(110)_\delta$ and propose an ad-hoc geometrical model explaining the passage from the δ-ferrite to the γ-austenite and finally to the K-$M_{23}C_6$.

This geometrical model, based on the corrugated layers [38,72–74], was developed to explain, among others things, the passage from the close-packed structures to the topologically close-packed (TCP) structures [44]. This approach emphasizes the necessity to consider corrugated compact layers instead of less dense lattice planes with the conservation of the site density at the interface plane [36,72–74]. This geometrical approach is especially proposed to account for the γ-austenite $\Rightarrow$ K-$M_{23}C_6$ transition.

To best understand the passage from one phase to the other one, the atomic distribution of the two phases is plotted using the CrystalMaker® software according to the cube-on-cube rational OR developed between the two phases. The atomic projection is recorded

along the common crystallographic direction $[\bar{1}10]$. Along this projection, the atomic planes parallel to (111) are edge-on and depicted by the straight parallel oblique lines (Figure 10a).

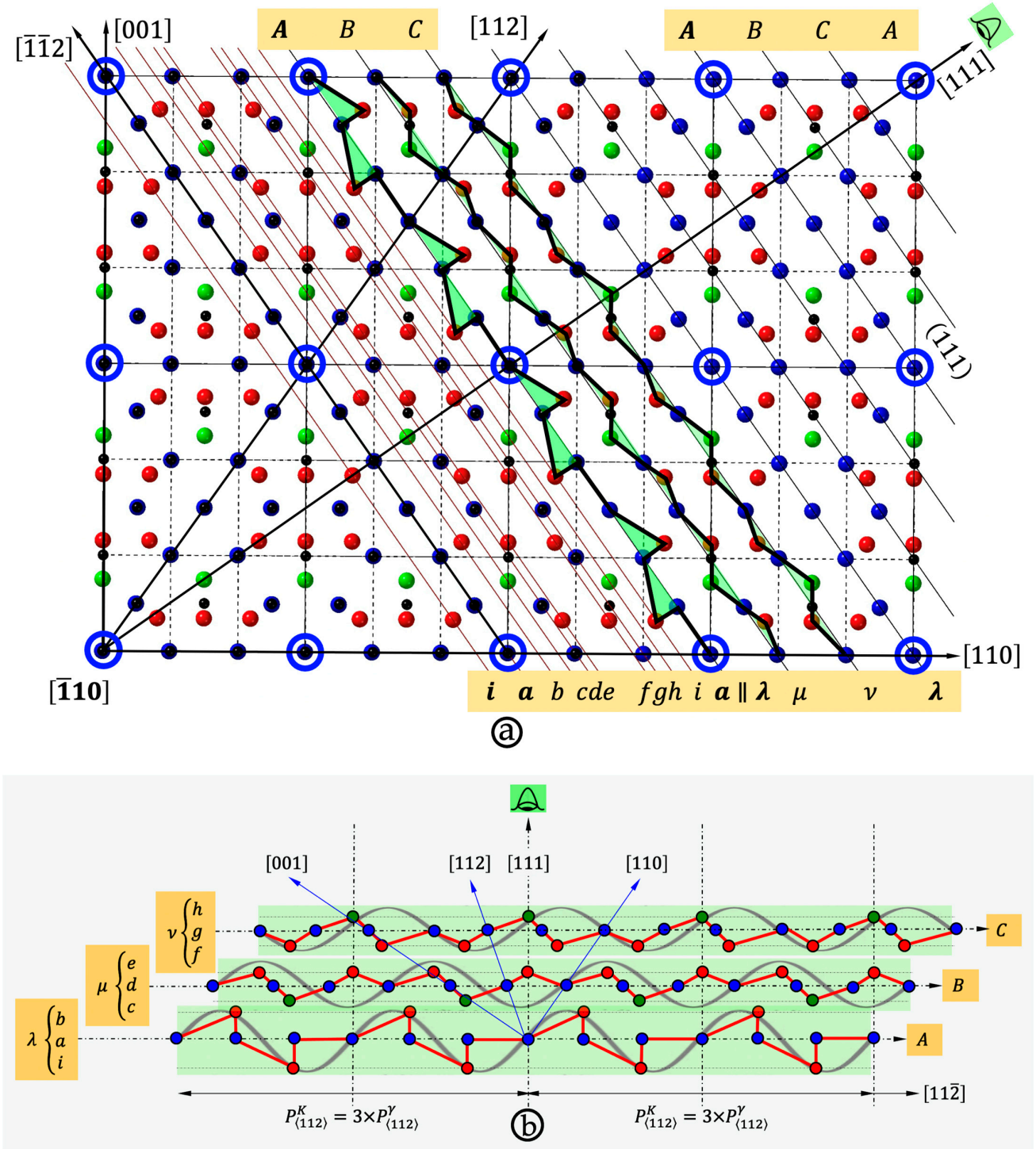

Figure 10. (**a**) Superimposition of the projection of the atomic structures of the austenite and of the K-carbide; the projection is recorded along $[\bar{1}10]$, (**b**) schematic representation showing how the 9 atomic planar layers $(i \rightarrow h)$ are grouped to form the 3 corrugated layers $(\lambda,\ \mu,\ \nu)$ of the K-carbide. The latter are grouped, respectively, around the 3 atomic planes $(A,\ B,\ C)$ of the γ-austenite. Both $(\lambda,\ \mu,\ \nu)$ and $(A,\ B,\ C)$ are observed edge-on. One can notice how the metallic atoms of the K-carbide are located on either side of the red zigzagged or grey corrugated layers. The black small atoms belong to the dashed lattice of the γ-austenite while the coloured ones belong to the K-lattice.

The black small atoms belong to the dashed lattice of the austenite while the coloured ones belong to the K-lattice. The nodes surrounded by blue empty circles correspond to coincident site lattices (CSL) dictated by the peculiarity of the lattice parameters and the cube-on-cube OR. For the sake of clarity, the carbon atoms ($4 \times 6 = 24$ carbon atoms related to the $4 \times 23 = 92$ metallic atoms entering in the constitution of the K-$M_{23}C_6$) were deliberately removed from these simulations. Only the Cr-metallic atoms are therefore taken into account (K-$Cr_{23}C_6$) in the representation of the atomic layers (Figures 10–13). The different colours refer to the 4 sites (a, c, f and h) occupied by the chromium atoms according to the Wyckoff notation [55,71].

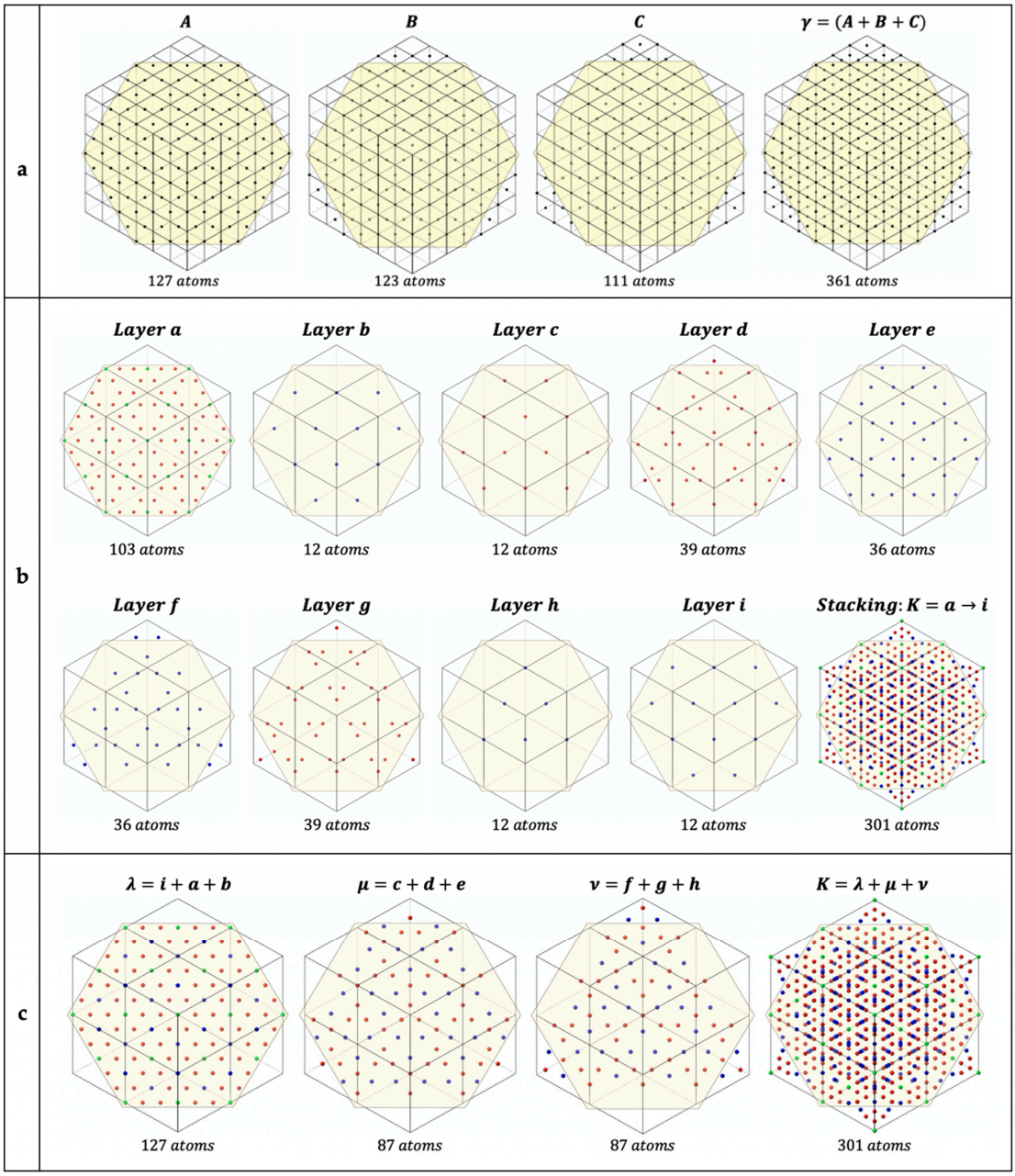

Figure 11. Projections along the [111] crystallographic direction showing the atomic distribution in (**a**) the 3 $(A,\ B,\ C)$ and (**b**) the 9 $(a \rightarrow i)$ atomic layers parallel to the (111) plane, describing the γ-austenite and the K-carbide, respectively. (**c**) Projection along the crystallographic $[111]_K \parallel [111]_\gamma$ showing the atomic distribution in the corrugated layers $(\lambda,\ \mu,\ \nu)$ of the K-carbide to be compared to that of the $(A,\ B,\ C)$ of the austenite. The compactness of the layers is given by the atomic number included in the external hexagonal surface. One observes that the atomic plane a is the densest one, followed by the atomic planes $d,\ e,\ f$ and g, while the less dense are $b,\ c,\ h$ and i $(b \equiv i)$.

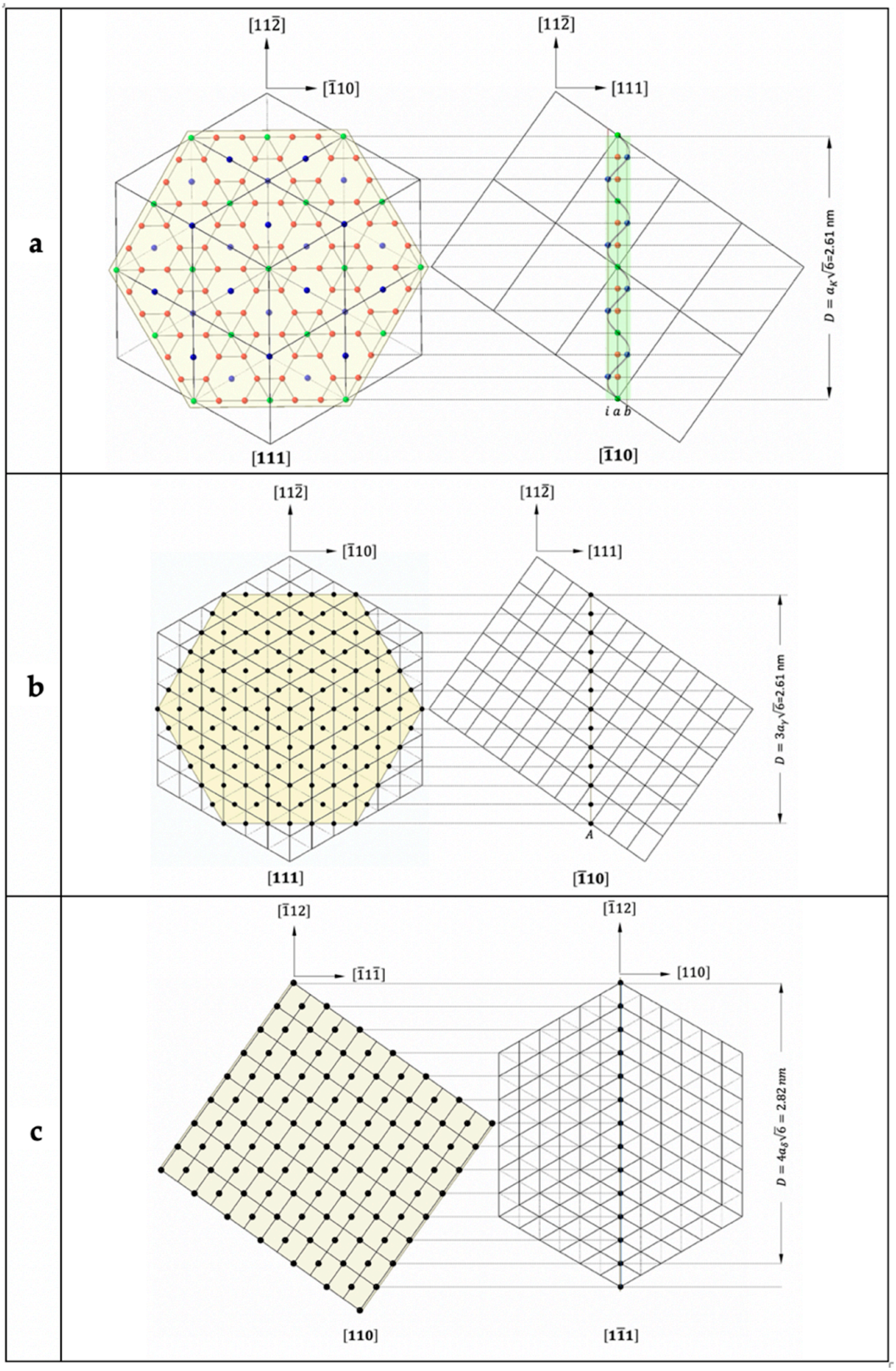

Figure 12. Flat and edge-on atomic projections of K-$M_{23}C_6$, γ-austenite and δ-ferrite phases, related by the TOR: (**a**,**b**) corrugated layer $\lambda = (i,\ a,\ b)$, and $\gamma = (111)$ along $[111]_{K,\ \gamma}$ and $[\bar{1}10]_{K,\ \gamma}$, (**c**) δ-ferrite along $[110]_\delta$ and $[1\bar{1}1]_\delta$ directions.

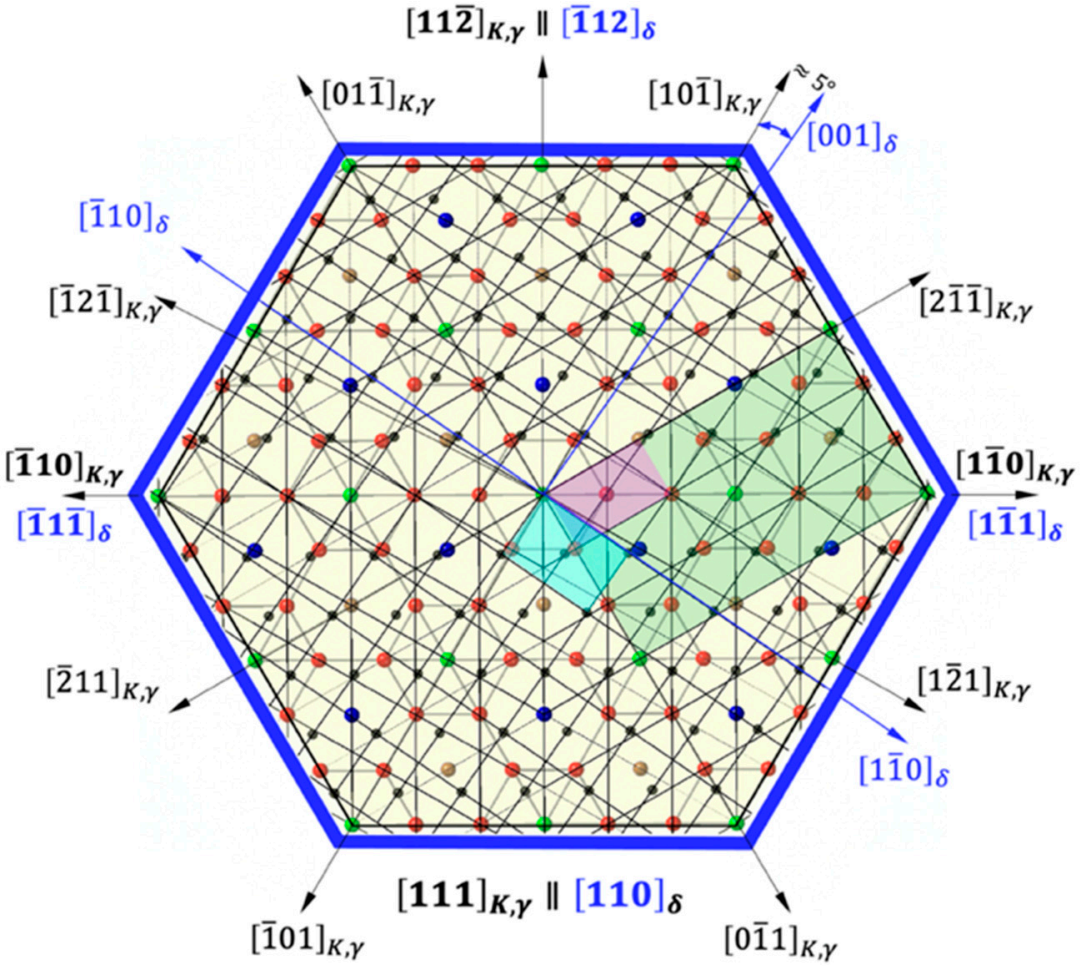

Figure 13. Superimposition of the densest parallel layers $(110)_{\delta}$ (small black dots), $(111)_{\gamma}$ and $(111)_{K,\gamma}$ (color dots) of δ-ferrite, γ-austenite and K-$M_{23}C_6$, respectively, obeying the triangular orientation relationship (TOR). The blue, red and green lattices correspond to the δ-ferrite, the γ-austenite and the K-$M_{23}C_6$, respectively.

Based on these simulations (Figure 10), and as it is expected, the γ-austenite can be described by 3 $(A,\ B,\ C)$ periodic close-packed planes stacked in the sequence $\gamma = (A,\ B,\ C)$ parallel to $(111)_{\gamma}$. However, the K-carbide can be described by 9 periodic atomic planes stacked in the sequence $K = (i, a,\ b, c, d, e, f, g,\ h) = (i\ \rightarrow h)$, parallel to $(111)_{K}$. The simulations recorded along $[111]_{\gamma} \parallel [111]_{K}$ (Figure 11) show the planes parallel to the sequences $\gamma = (A,\ B,\ C)$ and $K = (i \rightarrow h)$ parallel to $(111)_{\gamma}$ and $(111)_{K}$, respectively.

The interplanar spacing and the compactness of the atomic planes of the γ-austenite and of the $K = (i \rightarrow h)$ sequences are clearly displayed in Figures 10 and 11 and can thus be compared structurally. The compactness of a layer is given here by the atomic number included in the external hexagonal surface. The sequence $\gamma = (A,\ B,\ C)$ is characterised by constant interplanar spacing (Figure 10a) and by highest and constant atomic compactness of its planes (Figure 11a). As it is expected, one can point out $\frac{1}{3}[11\bar{2}]$ shifts between the stacked $(A,\ B,\ C)$ atomic layers, leading to a low compactness differential (Figure 10b).

Contrary to this $\gamma = (A,\ B,\ C)$ packing, the sequence $K = (i \rightarrow h)$ is distinguished by both atomic compactness and interplanar spacing whose values change from layer to layer (Figures 10 and 11). One observes, in the $K = (i \rightarrow h)$ sequence, that the atomic plane a is the densest one followed by the atomic planes $d,\ e,\ f$ and g, while the less dense are $b,\ c,\ h$ and i $(b \equiv i)$. The atomic organisation and atomic density of the plane a are similar to that of $(111)_{\gamma}$ (Figures 11 and 12) and $(110)_{\delta}$, (Figure 13).

To meet the requirement dictated by the geometrical model [38,72–74], (dense corrugated layers instead of less dense atomic planes, interface with high site density), the

9 $(i \rightarrow h)$ stacked atomic planes are gathered in 3 consecutive groups of atomic planes to form 3 periodic corrugated layers $K = (\lambda = iab,\ \mu = cde,\ \nu = fgh)$, in relation with the 3 atomic planes $(A,\ B,\ C)$ of the γ-austenite. Both $(\lambda,\ \mu,\ \nu)$ and $(A,\ B,\ C)$ are observed edge-on (Figure 10a,b). The straight oblique lines (Figure 10) are the traces of the (111) planes while the ziggzaged or wavy lines correspond to the traces of the corrugated layers parallel to the traces of the (111) planes (Figure 10b). One observes how the metallic atoms of the K-carbide are located on either side of the zigzagged or corrugated layers. The corrugated layers $K = (\lambda,\ \mu,\ \nu)$ are at the same mean inter-layer spacing, $\widetilde{d^{K}_{111}}$ ($\widetilde{d^{K}_{111}} = \frac{1}{9}d^{K}_{111} = \frac{1}{3}d^{\gamma}_{111} = 0.68$ A) and have more or less the same mean atomic density. These mean inter-layer spacings and mean atomic densities tend towards to that of the austenite as highlighted in Figure 11a,c.

Instead of describing the K-$M_{23}C_6$ by a stacking of planar layers like those for ferrite or austenite, we propose to describe it by a stacking of corrugated layers and not having the same atomic density. The stacking of the 3 atomic planes $(A,\ B,\ C)$ and the 3 corrugated layers $(\lambda,\ \mu,\ \nu)$ involve 361 atoms and 301 atoms, respectively. The difference of the site density between the two stacking is less than 17%. This compactness departure is to be linked to the carbon atoms which were not taken into account.

However, it is remarkable that the corrugated layer $\lambda\ (i + a + b)$ has exactly the same atomic density (Figure 11) as that of its corresponding A(111) atomic plane of the austenite, which moreover is close to that of the (110) plane of the ferrite. Then, the K/γ/δ potential interface implying the dense $(111)_{\gamma} \parallel (110)_{\delta}$ planes parallel to the corrugated layer $\lambda\ (i + a + b)$, realizes the conservation of the atomic sites density.

Such an approach, developed elsewhere [38,73,74], has already allowed the interpretation of interfaces developed between the topologically close packed (TCP) phases, σ and χ, taking place in the ferritic matrix.

When the corrugated layers concept is taken into account, the superimposition of the atomic projection along $[111]_{\gamma} \parallel [111]_{K}$ points out the similarity between the atomic distribution in the γ-austenite and in the K-carbide, allowing to explain the transition from one phase to the other one (Figure 13).

The triangular orientation relationship (TOR) developed between the three phases is best illustrated in Figure 13 by the superimposition of their densest planes $(111)_{K}//(111)_{\gamma}//(110)_{\delta}$ and maintaining the parallelism between the corresponding directions, namely:

$$[1\bar{1}0]_{K}//[1\bar{1}0]_{\gamma}//[1\bar{1}1]_{\delta}$$

$$[11\bar{2}]_{K}//[\bar{1}12]_{\gamma}//[\bar{1}12]_{\delta}$$

This schematic representation points out the similarity of the atomic distributions in the parallel densest planes dictated by the TOR, obeyed by the three phases. The passage from the ferrite network to that of the austenite/carbide would take place by atomic displacements whose amplitudes are smaller than the interatomic distances. One observes a lattice coherency for the three phases, with a misfit smaller than 1% (misfit: $\Delta^{[1\bar{1}0]_{K,\ \gamma} \parallel [1\bar{1}1]_{\delta}}_{K,\gamma,\delta} < 1$) along the common direction $[1\bar{1}0]_{K}//[1\bar{1}0]_{\gamma}//[1\bar{1}1]_{\delta}$. This crystallographic direction corresponds to the growth direction of the K-carbide in the ferritic matrix as indicated by the TEM observation (Figure 8).

3.7. Thermodynamic Analysis and Comments

The TCFE5 data base version of the thermodynamic ThermoCalq® software was used to calculate the stable phase equilibria for the 2205-DSS.

Figure 14 shows the predicted equilibrium mole fraction of K-$M_{23}C_6$ and σ-phase versus temperature. The mass percentage of all components entering in the composition of each of the two phases are superimposed. In Figure 14, the attention is only focused on K-$M_{23}C_6$ and σ-phase.

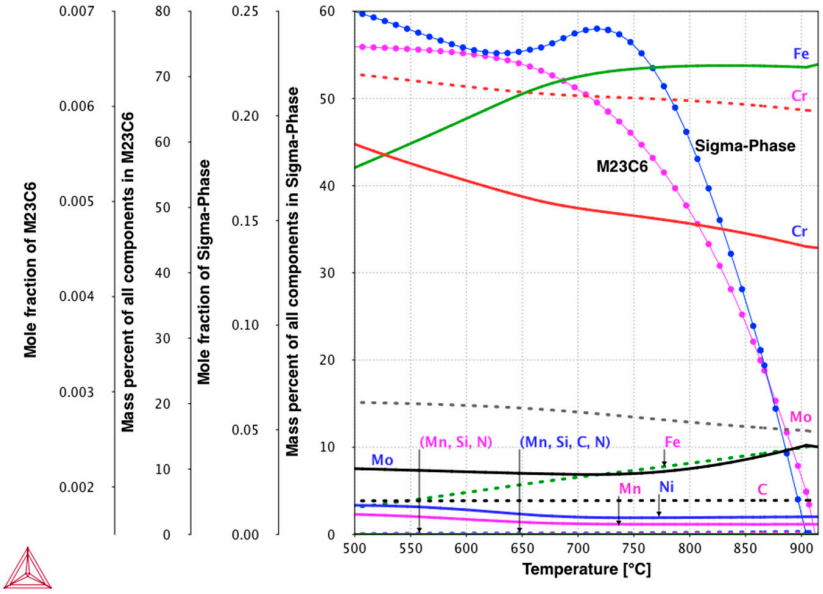

Figure 14. ThermoCalc® calculation plotted using the TCFE5 database for 2205-DSS, giving the mole fraction of phases and the mass percent of their alloying elements vs. temperature in the K-$M_{23}C_6$ and σ-phase, under equilibrium conditions. Dotted lines are concerned with the mole percent of alloying element in K-$M_{23}C_6$ while the continued lines are for those in the σ-phase.

According to this diagram, the appearance domains of σ-phase and of the K-$M_{23}C_6$ extend up to 904 and 936 °C, respectively. The two temperature domains almost overlap, this explains the concomitant presence of the two phases as indicated by the TEM investigation. In the temperature range 904–936 °C, the K-$M_{23}C_6$ appears in the δ-ferrite (essentially at the grain boundary) without accompanying the σ-phase, while they may be in the presence of austenitic islands.

At 500 °C, the temperature at which the mass fractions of the two phases are maximum, the K-$M_{23}C_6$ (0.7%) represents only 1% of the sigma phase (25%).

According to the diagram, it is quite clear that K-$M_{23}C_6$ mobilizes more Cr and Mo than $\sigma-$phase could do. Carbon, being insoluble in $\sigma-$phase, has the same level in the K-$M_{23}C_6$ throughout all the studied temperature range. On the other hand, $\sigma-$phase is richer in Ni and especially in Fe. This alloying element's distribution favours (promotes) the kinetics of the carbide at the expense of that of the $\sigma-$phase. In return, the K-$M_{23}C_6$ particles act as nucleation sites for $\sigma-$phase and even, of course, for the austenite. Therefore, the thermodynamic calculations developed previously are in agreement with the TEM observations.

4. Discussion

Through this study, a geometrical model, based on the corrugated compact layers instead of lattice planes with the conservation of the site density at the interface plane, has been proposed to explain the transition δ-ferrite ⇒ {γ-austenite ⇔ K-$M_{23}C_6$}.

To implement this geometrical model, the following balance sheet can be drawn to highlight the different steps:

- Identification of the potential interface shared by the engaged phases with respect to the OR: the densest planes dictated by the OR and with the conserved site density,
- Flat and edge-on representations of the atomic planes parallel the potential interface,
- Gathering atomic planes to form periodic corrugated layers based on the crystal structure, the compactness of the engaged atomic planes,
- Correspondence between the inter-layer spacing of the corrugated layer and the inter-reticular spacing of the corresponding atomic planes,

- Selection of the potential interface: The distance separating the corrugated carbide layers are the same as that of the inter-reticular spacing of the densest austenitic atomic planes. Selection of the corrugated layer distinguished by the close compactness as that of the densest austenitic atomic plane which is close to that of the densest atomic plane of the ferrite,
- Equilibrium shape: the coherency (CSL), potential growth direction (misfit),
- Passage: δ-ferrite ⇒ {γ-austenite ⇔ K-$M_{23}C_6$}.

This geometrical model can be generalised to explain the transitions from compact phases (fcc, bcc, hcp) to the topologically compact phases (TCP: sigma, G, R, chi, etc. phases).

Thermodynamic calculations, based on the commercial software ThermoCalq®, were carried out to explain the K-$M_{23}C_6$ precipitation and its effect on the other decomposition products of the ferritic matrix, namely γ-austenite and σ-phase. For this purpose, the mole fraction evolution of K-$M_{23}C_6$ and the σ-phase, and the mass percent of all components entering in their composition, have been drawn.

The mechanism involved in the formation of the lamellar (K-$M_{23}C_6$/γ-austenite)-aggregate is similar to that of the well-known lamellar pearlite, where the K-$M_{23}C_6$ carbide plays the role of Fe_3C-carbide, the cementite [75,76]. A $M_{23}C_6$ or γ-austenite nucleus takes place on the δ/δ grain boundary and its development modifies the chemical composition of the surrounding δ-ferritic matrix, which is depleted in ferrite and carbide stabilising elements (Cr, Mo, etc.) and enriched in austenite stabilising elements (Ni, Mn, etc.). This evolution of the chemical composition of the ferrite then promotes the formation of the austenite. This sequence reproduces along the δ/δ grain boundary leading to the lamellar K-$M_{23}C_6$/γ-austenite aggregate formation (Figure 9).

Since C the atoms necessary to form $M_{23}C_6$ are supplied from the area surrounding the native (K-$M_{23}C_6$/γ-austenite)-eutectoid, the amount of C atoms supplied will decrease with the progress of aging time and the reaction will finally stop.

5. Conclusions

Through this study, it was shown that depending on the heat treatments, isothermal or anisothermal, the K-$M_{23}C_6$ precipitates as particles at the δ/δ grain boundaries or as lamellae in (K-$M_{23}C_6$/γ)-eutectoid, respectively. Whatever the holding temperature, the K-$M_{23}C_6$ formation points ahead those of γ-austenite and σ-phase, by acting as highly potential nucleation sites. This result is supported by TEM observation and thermodynamic calculations. However, during the anisothermal heat treatment, the K-$M_{23}C_6$ precipitates as alternated lamellae with the austenite, forming an eutectoid. The crystal structure of the K-$M_{23}C_6$ was determined by microdiffraction. The $Fm\bar{3}m$ space group and the lattice parameter ($a_K = 1.0645$ nm) are in accordance with those reported in the literature. The K-$M_{23}C_6$ adopts a cube-on-cube orientation relationship with the austenitic lamellae, which adopts a Kurdjumov-Sachs relation with the ferritic matrix. The K-$M_{23}C_6$ develops only one variant inside each eutectoid island among the 24 developed in the ferrite. This result is supported by symmetry analysis.

Author Contributions: Conceptualization, A.R. and A.M.M.G.; methodology, A.R. and A.M.M.G.; software, A.R.; validation, A.R. and A.M.M.G.; writing—original draft preparation, A.R.; writing—review and editing, A.R. and A.M.M.G.; project administration, A.R. All authors have read and agreed to the published version of the manuscript.

Funding: A.M.M.G. acknowledges the Direcció General de Recerca del Comissionat per a Universitats I Recerca de la Generalitat de Catalunya for recognizing CIEFMA as a consolidated Research Group (2017SGR33).

Conflicts of Interest: The authors declare no conflict of interest.

References

1. Davison, R.M.; Redmond, J.D. Practical guide to using duplex stainless steels. *Mater. Perform.* **1990**, *29*, 57–62.
2. Diggs, V.J.; Busko, W.D.; Schillmoller, C.M. The role of duplex stainless steels in the oil and gas industry. In *Proceedings of the International Conference on Duplex Stainless Steels '91, Bourgogne, France, 28–30 October 1991*; Charles, J., Bernhardsson, S., Eds.; Les Editions de Physique: Les Ulis, France, 1991; Volume 2, pp. 1163–1185.
3. Fruytier, D.J.A. Industrial experience with duplex stainless steel related to their specific properties. In *Proceedings of the International Conference on Duplex Stainless Steels'91, Bourgogne, France, 28–30 October 1991*; Charles, J., Bernhardsson, S., Eds.; Les Editions de Physique: Les Ulis, France, 1991; Volume 2, pp. 497–508.
4. Jebaraj, A.V.; Ajaykumar, L.; Deepak, C.; Aditya, K. Weldability, machinability and surfacing of commercial duplex stainless steel AISI2205 for marine applications – A recent review. *J. Adv. Res.* **2017**, *8*, 183–199. [CrossRef] [PubMed]
5. Tamura, I.; Tomota, Y. Presented at Symposium on Mechanical Behaviour of Materials, Kyoto, Japan, 21–24 August 1974.
6. Foct, J.; Akdut, N.; Gottstein, G. Why are "duplex" microstructures easier to form than expected? *Scr. Met. Mater.* **1992**, *27*, 1033–1038. [CrossRef]
7. Sridhar, N.; Kolts, J.H.; Flasche, L.H. A Duplex Stainless Steel for Chloride Environments. *JOM* **1985**, *37*, 31–35. [CrossRef]
8. Magnin, T.; Lardon, J. Cyclic deformation mechanisms of a two-phase stainless steel in various environmental conditions. *Mater. Sci. Eng. A* **1988**, *104*, 21–28. [CrossRef]
9. Bernhardsson, S.; Oredsson, J.; Martenson, C. The stress corrosion cracking resistance of duplex stainless steels in chloride environments. In *Proceedings of the International Conference on Duplex Stainless Steels'82*; Lula, R.A., Ed.; ASM: Metals Park, OH, USA, 1983; pp. 267–281.
10. Prouheze, J.C.; Vaillant, J.C.; Guntz, G.; Lefebvre, B. Production of tubing in duplex stainless steels VS22 influence of cold work on mechanical properties–Behaviour in corrosive sour gas and oil environment. In *Proceedings of the International Conference on Duplex Stainless Steels'82*; Lula, R.A., Ed.; ASM: Metals Park, OH, USA, 1983; p. 247.
11. Westgren, A. Complex Chromium and Iron Carbides. *Nat. Cell Biol.* **1933**, *132*, 480. [CrossRef]
12. Goldschmidt, H.J. A New Carbide in Chromium Steels. *Nat. Cell Biol.* **1948**, *162*, 855–856. [CrossRef]
13. Bowman, A.L.; Arnold, G.P.; Storms, E.K.; Nereson, N.G. The crystal structure of Cr23C6. *Acta Crystallogr. Sect. B Struct. Crystallogr. Cryst. Chem.* **1972**, *28*, 3102–3103. [CrossRef]
14. Solomon, H.D. Age hardening in a duplex stainless steel. In *Proceedings of the International Conference on Duplex Stainless Steels'82*; Lula, R.A., Ed.; ASM: Metals Park, OH, USA, 1983; p. 41.
15. Southwick, P.D.; Honeycombe, R.W.K. Precipitation of $M_{23}C_6$ at austenite/ferrite interfaces in duplex stainless steel. *Met. Sci.* **1982**, *16*, 475–482. [CrossRef]
16. Maetz, J.-Y.; Douillard, T.; Cazottes, S.; Verdu, C.; Kléber, X. $M_{23}C_6$ carbides and Cr2N nitrides in aged duplex stainless steel: A SEM, TEM and FIB tomography investigation. *Micron* **2016**, *84*, 43–53. [CrossRef] [PubMed]
17. Southwick, P.D.; Honeycombe, R.W.K. Decomposition of ferrite to austenite in 26%Cr-5%Ni stainless steel. *Met. Sci.* **1980**, *14*, 253–261. [CrossRef]
18. Charles, J. Super duplex stainless steels: Structure and properties. In *Proceedings of the International Conference on Duplex Stainless Steels '91, Bourgogne, France, 28–30 October 1991*; Charles, J., Bernhardsson, S., Eds.; Les Editions de Physique: Les Ulis, France, 1991; Volume 2, pp. 3–48.
19. Redjaïmia, A.; Metauer, G.; Gantois, M. Decomposition of Delta Ferrite in a Fe-22Cr-5Ni-3Mo-0.03C Duplex Stainless Steel. A morphological and Structural Study. In *Proceedings of the International Conference on Duplex Stainless Steels '91, Bourgogne, France, 28–30 October 1991*; Charles, J., Bernhardsson, S., Eds.; Les Editions de Physique: Les Ulis, France, 1991; Volume 2, pp. 120–134.
20. Redjaïmia, A.; Metauer, G.; Gantois, M. Isothermal decomposition of delta ferrite in Fe-22Cr-5Ni-3Mo-0.03C stainless steel. In *Proceedings of the Eighth International on Offshore Mechanics and Arctic Engineering Symposium, The Hague, The Netherlands, 19–23 March 1989*; Salama, M., Bangaru, N.V., Denys, R., Rhee, H.C., Toyoda, M., Eds.; The ASME: New York, NY, USA, 1989; Volume 3, pp. 179–185.
21. Redjaïmia, A.; Metauer, G. Diffusion controlled precipitation of austenitic bi-crystals possessing twin related orientation in the ferrite of a duplex stainless steel. *J. Mater. Sci.* **2001**, *36*, 1717–1725. [CrossRef]
22. Redjaimia, A.; Metauer, G.; Gantois, M. Morphologie et structure de la phase α' formée dans un acier duplex Z 3 CND 22-05. *Scr. Met. Mater.* **1991**, *25*, 1879–1882. [CrossRef]
23. Örnek, C.; Idris, S.A.; Reccagni, P.; Engelberg, D.L. Atmospheric-Induced Stress Corrosion Cracking of Grade 2205 Duplex Stainless Steel—Effects of 475 °C Embrittlement and Process Orientation. *Metals* **2016**, *6*, 167. [CrossRef]
24. Fargas, G.; Anglada, M.; Mateo, A. Effect of the annealing temperature on the mechanical properties, formability and corrosion resistance of hot-rolled duplex stainless steel. *J. Mater. Process. Technol.* **2009**, *209*, 1770–1782. [CrossRef]
25. Llanes, L.; Mateo, A.; Iturgoyen, L.; Anglada, M. Aging effects on the cyclic deformation mechanisms of a duplex stainless steel. *Acta Mater.* **1996**, *44*, 3967–3978. [CrossRef]
26. Beattie, H.J.; Versnyder, F.L. A New Complex Phase in a High-Temperature Alloy. *Nat. Cell Biol.* **1956**, *178*, 208–209. [CrossRef]
27. Mateo, A.; Llanes, L.; Anglada, M.; Redjaimia, A.; Metauer, G. Characterization of the intermetallic G-phase in an AISI 329 duplex stainless steel. *J. Mater. Sci.* **1997**, *32*, 4533–4540. [CrossRef]

28. Redjaïmia, A.; Ruterana, P.; Metauer, G.; Gantois, M. Identification et caractérisation d'une nouvelle phase intermétallique dans un acier inoxydable austéno-ferritique Z3CND22-05. In Proceedings of the Coloquio Franco-Ibérico de Microscopia Electronica, Barcelona, Spain, 4–7 December 1991; pp. 382–383, ISBN 84-7875-707-4.
29. Redjaimia, A.; Ruterana, P.; Metauer, G.; Gantois, M. Identification and characterization of a novel intermetallic compound in a Fe-22 wt % Cr-5 wt % Ni-3 wt % Mo-0.03 wt % C duplex stainless steel. *Philos. Mag. A* **1993**, *67*, 1277–1286. [CrossRef]
30. Ruterana, P.; Redjaïmia, A. Microdiffraction, EDS, and HREM investigation for phase identification with the electron microscope. *Proc. Mater. Res. Soc. Symp.* **2000**, *589*, 161–166. [CrossRef]
31. Treitschke, W.; Tammann, G. Enthalpy of formation for σ-phase solid solutions at 1060 K. *Anorg. Chem.* **1907**, *55*, 707–708.
32. Bain, E.C.; Griffiths, W.E. An introduction to the iron-chromium-nickel alloys. *Trans. AIME* **1927**, *75*, 166–213.
33. Bergman, G.; Shoemaker, D.P. The determination of the crystal structure of the σ phase in the iron–chromium and iron–molybdenum systems. *Acta Crystallogr.* **1954**, *7*, 857–865. [CrossRef]
34. Kasper, J.S.; Waterstrat, R.M. Ordering of atoms in the σ phase. *Acta Crystallogr.* **1956**, *9*, 289–295. [CrossRef]
35. Koutsoukis, T.; Redjaïmia, A.; Fourlaris, G. Phase transformations and mechanical properties in heat treated superaustenitic stainless steels. *Mater. Sci. Eng. A* **2013**, *561*, 477–485. [CrossRef]
36. Andrews, K.W. A New Intermetallic Phase in Alloy Steels. *Nat. Cell Biol.* **1949**, *164*, 1015. [CrossRef]
37. Kasper, J. The ordering of atoms in the chi-phase of the iron-chromium-molybdenum system. *Acta Met.* **1954**, *2*, 456–461. [CrossRef]
38. Redjaïmia, A.; Proult, A.; Donnadieu, P.; Morniroli, J.P. Morphology, crystallography and defects of the intermetallic -phase precipitated in a duplex (+) stainless steel. *J. Mater. Sci.* **2004**, *39*, 2371–2386. [CrossRef]
39. Ohmori, Y.; Maehara, Y. Precipitation of $M_{23}C_6$ and σ-phase in δ/γ Duplex Stainless Steels. *Trans. ISIJ* **1984**, *24*, 60–68. [CrossRef]
40. Rideout, S.; Manly, W.D.; Kamen, E.L.; Lement, B.S.; Beck, P.A. Intermediate Phases in Ternary Alloy Systems of Transition Elements. *JOM* **1951**, *3*, 872–876. [CrossRef]
41. Komura, Y.; Sly, W.G.; Shoemaker, D.P. The crystal structure of the R phase, Mo–Co–Cr. *Acta Crystallogr.* **1960**, *13*, 575–585. [CrossRef]
42. Shoemaker, C.B.; Fox, A.H.; Mellor, J. Neutron diffraction studies of the order of the atoms in the P phase and the R phase. *Acta Crystallogr.* **1965**, *18*, 37–44. [CrossRef]
43. Redjaïmia, A.; Morniroli, J.P.; Donnadieu, P.; Metauer, G. Microstructural and analytical study of heavily faulted Frank-Kasper R-phase precipitates in the ferrite of a duplex stainless steel. *J. Mater. Sci.* **2002**, *37*, 4079–4091. [CrossRef]
44. Frank, F.C.; Kasper, J.S. Complex alloy structures regarded as sphere packings. I. Definitions and basic principles. *Acta Crystallogr.* **1958**, *11*, 184–190. [CrossRef]
45. Steeds, J.W.; Evans, N.S. *Proceedings of the 38th Annual EMSA Meeting*; Bailey, G.W., Ed.; Claitor's: Baton Rouge, LA, USA, 1981; pp. 188–191.
46. Raghavan, M.; Koo, J.Y.; Petkovic-Luton, R. Some Applications of Convergent Beam Electron Diffraction in Metallurgical Research. *JOM* **1983**, *35*, 44–50. [CrossRef]
47. Steeds, J.W.; Vincent, R. Use of high-symmetry zone axes in electron diffraction in determining crystal point and space groups. *J. Appl. Crystallogr.* **1983**, *16*, 317–324. [CrossRef]
48. Raghavan, M.; Scanlon, J.C.; Steeds, J.W. Use of Reciprocal Lattice Layer Spacing in Convergent Beam Electron Diffraction Analysis. *Met. Mater. Trans. A* **1984**, *15*, 1299–1302. [CrossRef]
49. Ayer, R.; Scanlon, J.C.; Ramanarayanan, T.A.; Mueller, R.R.; Petkovic-Luton, R.; Steeds, J.W. Crystal structure of intermetallic phase in Fe–20Cr–4Al–0.5Y alloy by convergent beam electron diffraction. *J. Mater. Res.* **1987**, *2*, 16–27. [CrossRef]
50. Morniroli, J.; Steeds, J. Microdiffraction as a tool for crystal structure identification and determination. *Ultramicroscopy* **1992**, *45*, 219–239. [CrossRef]
51. Redjaïmia, A.; Morniroli, J. Application of microdiffraction to crystal structure identification. *Ultramicroscopy* **1994**, *53*, 305–317. [CrossRef]
52. Morniroli, J.; Redjaïmia, A.; Nicolopoulos, S. Contribution of electron precession to the identification of the space group from microdiffraction patterns. *Ultramicroscopy* **2007**, *107*, 514–522. [CrossRef] [PubMed]
53. Buerger, M.J. *Elementary Crystallography*; Massachusetts Institute of Technology Press: Cambridge, UK, 1978.
54. Phillips, F.C. *An Introduction to Crystallography*, 4th ed.; Longman: Singapore, 1971.
55. Hahn, T. *International Tables for Crystallography*; Reidel: Dordrecht, The Netherlands, 1988.
56. Kurdjumow, G.; Sachs, G. Über den Mechanismus der Stahlhärtung. *Eur. Phys. J. A* **1930**, *64*, 325–343. [CrossRef]
57. Cahn, J.W.; Kalonji, G. *Proceedings of the International Conference on Solid-Solid Phase Transformations*; Aaronson, H.I., Sekereka, R.F., Laughlin, D.E., Waymann, C.M., Eds.; AIME Press: Warendale, PA, USA, 1982; pp. 3–14.
58. Portier, R.; Gratias, D. Symmetry and phase transformation. *J. Phys. Suppl.* **1982**, *43*, C4–C17. [CrossRef]
59. Muddle, B.; Polmear, I. The precipitate Ω phase in Al-Cu-Mg-Ag alloys. *Acta Met.* **1989**, *37*, 777–789. [CrossRef]
60. Hugo, G.; Muddle, B. The morphology of precipitates in an Al Ge alloy—II. Analysis using symmetry. *Acta Met. Mater.* **1990**, *38*, 365–374. [CrossRef]
61. Boudeulle, M. Disproportionation in mineral solid solutions: Symmetry constraints on precipitate orientation and morphology. Implications for the study of oriented intergrowths. *J. Appl. Crystallogr.* **1994**, *27*, 567–573. [CrossRef]

62. Gouné, M.; Redjaïmia, A.; Belmonte, T.; Michel, H. Identification and characterization of a novel Mn-N nitride formed in Fe-Mn-N alloy. *J. Appl. Crystallogr.* **2003**, *36*, 103–108. [CrossRef]
63. Skiba, O.; Redjaïmia, A.; Dulcy, J.; Ghanbaja, J.; Marcos, G.; Caldeira-Meulnotte, N.; Czerwiec, T. A proper assessment of TEM diffraction patterns originating from CrN nitrides in a ferritic matrix. *Mater. Charact.* **2018**, *144*, 671–677. [CrossRef]
64. Kabbara, H.; Ghanbaja, J.; Redjaïmia, A.; Belmonte, T. Crystal structure, morphology and formation mechanism of a novel polymorph of lead dioxide, γ-PbO2. *J. Appl. Crystallogr.* **2019**, *52*, 304–311. [CrossRef]
65. Ozturk, U.; Cabrera, J.M.; Calvo, J.; Redjaïmia, A.; Ghanbaja, J. High-Temperature Deformation Behavior of 718Plus: Consideration of γ′ Effects. *Mater. Perform. Charact.* **2020**, *9*, 57–74. [CrossRef]
66. Chung, T.-F.; Yang, Y.-L.; Shiojiri, M.; Hsiao, C.-N.; Li, W.-C.; Tsao, C.-S.; Shi, Z.; Lin, J.; Yang, J.-R. An atomic scale structural investigation of nanometre-sized η precipitates in the 7050 aluminium alloy. *Acta Mater.* **2019**, *174*, 351–368. [CrossRef]
67. Souissi, M.; Sluiter, M.H.F.; Matsunaga, T.; Tabuchi, M.; Mills, M.J.; Sahara, R. Effect of mixed partial occupation of metal sites on the phase stability of γ-Cr23-xFe x C6 (x = 0-3) carbides. *Sci. Rep.* **2018**, *8*, 7279. [CrossRef]
68. Kuo, K.; Jia, C. Crystallography of $M_{23}C_6$ and M_6C precipitated in a low alloy steel. *Acta Met.* **1985**, *33*, 991–996. [CrossRef]
69. Henry, G.; Maitrepierre, P.; Michaut, B.; Thomas, B. Cinétique et morphologie de la précipitation intergranulaire de borocarbures m23(b, c)6 dans les aciers. *J. Phys. Colloq.* **1975**, *36*, C4–C245. [CrossRef]
70. Beckitt, F.; Clark, B. The shape and mechanism of formation of $M_{23}C_6$ carbide in austenite. *Acta Met.* **1967**, *15*, 113–129. [CrossRef]
71. Li, Z.; Hou, T.; Wu, G.; Wu, K.; Lin, H. Thermodynamic Analysis for the Magnetic-Field-Induced Precipitation Behaviours in Steels. *Metals* **2019**, *9*, 909. [CrossRef]
72. Duneau, M.; Oguey, C. Bounded interpolations between lattices. *J. Phys. A Math. Gen.* **1991**, *24*, 461–475. [CrossRef]
73. Proult, A.; Donnadieu, P. A simple description of the α-manganese (A12) structure derived from defect studies. *Philos. Mag. Lett.* **1995**, *72*, 337–344. [CrossRef]
74. Proult, A.; Redjaimia, A.; Donnadieu, P. Interface Between Simple Crystal and Icosahedral-Symmetry Related Crystal. *J. Phys. Colloq.* **1996**, *06*, C2–C135. [CrossRef]
75. Madeleine Prof. Dr ès Sciences Madeleine Durand-Charre The pearlite transformation. In *Polymer-Engineered Nanostructures for Advanced Energy Applications*; Springer Science and Business Media LLC: Berlin/Heidelberg, Germany, 2004; pp. 195–208.
76. Xiong, X.C.; Redjaimia, A.; Gouné, M. Pearlite in hypoeutectoid iron-nitrogen binary alloys. *J. Mater. Sci.* **2009**, *44*, 632–638. [CrossRef]